Design of Dynamic Inversion and Explicit Model Following Flight Control Laws for Quadrotor UAS

Umberto Saetti*	Joseph F. Horn	Sagar Lakhmani	Constantino Lagoa	Tom Berger
Graduate Assistant	*Professor*	*Graduate Assistant*	*Professor*	*Aerospace Engineer*
Department of Aerospace Engineering		*Department of Electrical Engineering*		*U.S. Army Aviation*
The Pennsylvania State University		*The Pennsylvania State University*		*Development Directorate*
University Park, PA		*University Park, PA*		*Moffett Field, CA*

The objectives of this paper are to advance dynamic inversion (DI) and explicit model following (EMF) flight control laws for quadrotor unmanned aerial systems (UAS) and to develop an efficient strategy to compute the stability and performance robustness statistics of such control laws given parametric model uncertainty. For this purpose, a parametric model of a quadrotor is identified from flight-test data. The identified model is validated both in frequency and time domains. Next, DI and EMF flight control laws are designed for both inner attitude and outer velocity loops. Finally, a novel approach based on an unsicented transform is used to evaluate the statistics of the controller's performance based on the statistics of the uncertain model parameters.

Nomenclature

$\mathbf{A},\mathbf{B},\mathbf{C}$	state, control, and output matrices
$\hat{\mathbf{A}}, \hat{\mathbf{B}}$	modified state and control matrices
$\mathbf{e}$	error vector
g	gravitational acceleration
$\mathscr{H}$	parameter identification Hessian matrix
J	average system identification cost function
$\mathbf{K}_D, \mathbf{K}_I, \mathbf{K}_P$	derivative, integral, and proportional gain matrices
$L_v, L_{\delta\text{lat}}, Y_v, Y_{\delta\text{lat}}$	lateral stability and control derivatives
$M_u, M_{\delta\text{lon}}, X_u, X_{\delta\text{lon}}$	longitudinal stability and control derivatives
$N_r, N_{\delta\text{dir}}$	directional stability and control derivatives
P	covariance matrix
p, q, r	roll, pitch, and yaw rates
$\mathbf{T}_{h/b}$	rotational matrix from body to heading frame
$\mathbf{u}, \mathbf{x}, \mathbf{y}$	input, state, and output vectors
u, v, w	velocities in body frame
V_x, V_y, V_z	heading frame velocities
$\hat{\mathbf{x}}$	modified state vector
$Z_w, Z_{\delta\text{col}}$	heave stability and control derivatives
$\delta_{\text{lat}}, \delta_{\text{lon}}, \delta_{\text{col}}, \delta_{\text{ped}}$	lateral, longitudinal, and collective sticks, and pedal
ν	pseudo-command vector
ρ	relative weighting between the control and state penalties
τ	command model time constant
$\tau_\phi, \tau_\theta, \tau_\psi, \tau_z$	equivalent time delays
ϕ, θ, ψ	Euler angles
ω_n	command model natural frequency

Subscript

cmd	reference trajectory

Introduction

Small-scale quadrotor unmanned aerial systems (UAS) are particularly prone to gust disturbances and therefore need flight control systems able to mitigate this deficiency. Model following control architectures such as dynamic inversion (DI) and explicit model following (EMF) are especially well-suited for providing gust disturbance rejection. This is because their 2 degree-of-freedom (DOF) structure, with separate feed forward and feedback paths, allows tuning the UAS response to gusts independently from responses to outer guidance/navigation loops. In contrast, in 1 DOF classic control methodologies, the responses to gusts and outer guidance/navigation loops cannot be independently tuned. A key aspect of both architectures is the reliance on model inversion to cancel the plant dynamics and track a desired reference model. EMF is essentially a linear design method that uses a simplified model inversion in the feed-forward path to follow the desired reference model, whereas feedback design is applied to the high-order linear plant models that are either identified from flight-test data or obtained from physics-based models via linearization schemes. Generally, both feed-forward inversion and feedback compensation need to be scheduled with the flight condition to account variations in the flight dynamics. DI, on the other hand, inverts the plant model in its feedback linearization loop, which eliminates the need for gain scheduling. However, the plant model used for feedback linearization still needs to be scheduled with the flight

condition. The development of DI flight control laws for rotorcraft has been a major area of research at the Pennsylvania State University over the past two decades. The majority of these studies concentrated on full-scale rotorcraft [1–8], whereas only a few focused on small-scale UAS [9, 10]. Further, the studies that focused on small-scale quadrotors only implemented DI for outer guidance/navigation loops and relied on the UAS built-in controllers for the inner attitude loops. On the other hand, the U.S. Army Aviation Development Directorate has been mostly active in the advancement of EMF flight controls laws for aircraft and rotorcraft across all scales [11–15]. Although a significant amount of published research is available on the design of DI and EMF flight controllers, these two methodologies were not yet tied together to produce equivalent control laws for small-scale quadrotor UAS.

A key requirement in the design of UAS flight control laws is that the aircraft meet quantitative stability and performance requirements. Evaluation of these criteria involves the use of linear models derived either through flight-test data or by linearizing nonlinear physics-based models. Because such linear model are generally subject to parametric uncertainty, quantitative stability and performance assessment based on the linear models are subject to uncertainty as well. In the specific case where the linear model uncertainty is significant, deterministic judgments about a vehicle's conformance to stability and performance specifications may not be accurate or sufficient. Rather, probabilistic assessments must be made in which it may be stated that the vehicle conforms to specific guidelines with a certain probability, given the uncertainty in the vehicle closed-loop dynamics. For this reason, there is a need for new methodologies that can propagate parametric uncertainty in the aircraft model to the stability and performance assessments. A few published research studies exist in this area and are almost exclusively based on Monte Carlo dispersions [11, 16, 17]. While of easy implementation, Monte Carlo suffers from well-known scalability issues such that the number of samples needed to generate sufficient accuracy may become prohibitively high as the dimensionality of the uncertainty increases. This is a significant potential problem in UAS flight control system design where numerous plant parameters are typically subject to uncertainty. For this reason, a new methodology based on an unscented transform [18] is developed to evaluate the statistics of the controller performance based on the statistics of the uncertain model parameters. The unscented transform approach is chosen because it requires fewer data points than Monte Carlo and is therefore computationally more efficient.

The objectives of this research are twofold. The first objective is to advance the design of DI and EMF flight controls laws for quadrotor UAS. The second objective is to develop a new methodology based on an unscented transform to evaluate the statistics of the controllers performance based on the statistics of the uncertain model parameters. For this purpose, a parametric model of a quadrotor assembled with commercial off-the-shelf components is identified from flight-test data using a frequency-domain approach.

This paper presents an overview of the hardware used on the quadrotor, as well as the results of system identification performed on the quadrotor. Next, the synthesis of DI and EMF control laws for both an inner attitude and outer velocity loops is presented. The performance of the DI and EMF controllers is compared both in time and frequency domains. In addition, a novel approach based on an unscented transform is developed and used to evaluate stability and performance robustness statistics from the identified bare-airframe parameters uncertainty statistics. Finally, conclusions are presented.

Hardware Overview

The in-house quadrotor, shown in Fig. 1, is comprised of four main components: on-board computer, flight controller, sensors, and electric
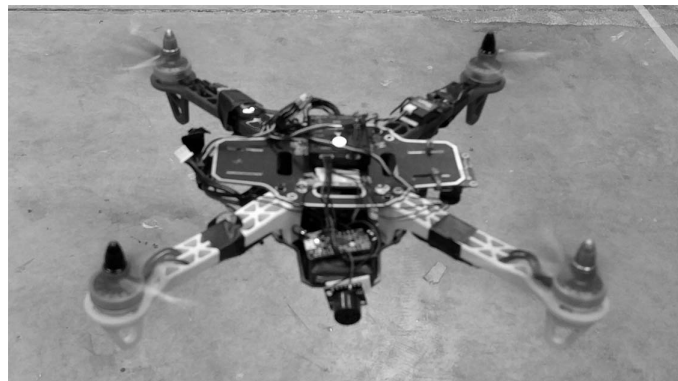

Fig. 1. Quadrotor UAS.

motors. The flight controller used is the PixHawk, which is responsible for running the built-in control algorithm. The control algorithm allows to switch between manual flight using the remote controller or an automated flight whenever the pilot needs to. The flight controller has a built-in inertial measurement unit, a gyroscope, a GPS receiver, and a barometer used to determine the changes in altitude. A ground station (GS) and transmitter are also incorporated into the control architecture of the UAS. The GS is primarily used for monitoring the telemetry data during flight.

Parametric Identification

System identification is done in two steps using the CIFER® [19] software tool. The identification procedure is based on the use of frequency responses. First, frequency responses of the aircraft output are extracted from frequency–sweep flight data. Next, state-space models are identified from the frequency response data. A frequency-domain filtering approach is used. Time-domain identification techniques that require integration of the equations of motion would not work well for the hovering quadrotor since the system is unstable, and the instability is at a relatively high frequency (i.e., the frequency of the unstable hovering cubic). This would lead to a quick divergence of the model integration, forcing to use very short record lengths for the identification. Frequency sweeps in different channels are performed on each axis, separately. The axes in consideration are roll, pitch, yaw, and heave. Piloted frequency sweeps are used rather than automated inputs due to their excellent broadband excitation [19]. The built-in controller is activated during the system identification process to ensure the quadrotor stability and therefore ease the task of the pilot in performing the sweeps. A schematic of the quadrotor control system is shown in Fig. 2. Given the largely decoupled dynamics in each axis around hover, which is due to the symmetry of the configuration, system identification is performed separately around each axis.

Lateral dynamics

The lateral state-space model structure and relative output equations are, respectively,

$$
\begin{bmatrix} \dot{v} \\ \dot{p} \\ \dot{\phi} \end{bmatrix} = \begin{bmatrix} Y_v & 0 & g \\ L_v & L_p & 0 \\ 0 & 1 & 0 \end{bmatrix} \begin{bmatrix} v \\ p \\ \phi \end{bmatrix} + \begin{bmatrix} 0 \\ L_{\delta_{\text{lat}}} \\ 0 \end{bmatrix} \delta_{\text{lat}}(t - \tau_\phi) \tag{1a}
$$

$$
\begin{bmatrix} \dot{v} \\ p \\ a_y \end{bmatrix} = \begin{bmatrix} Y_v & 0 & g \\ 0 & 1 & 0 \\ Y_v & 0 & 0 \end{bmatrix} \begin{bmatrix} v \\ p \\ \phi \end{bmatrix} \tag{1b}
$$

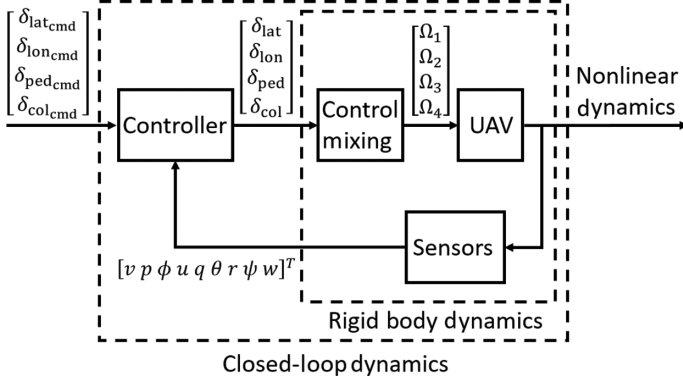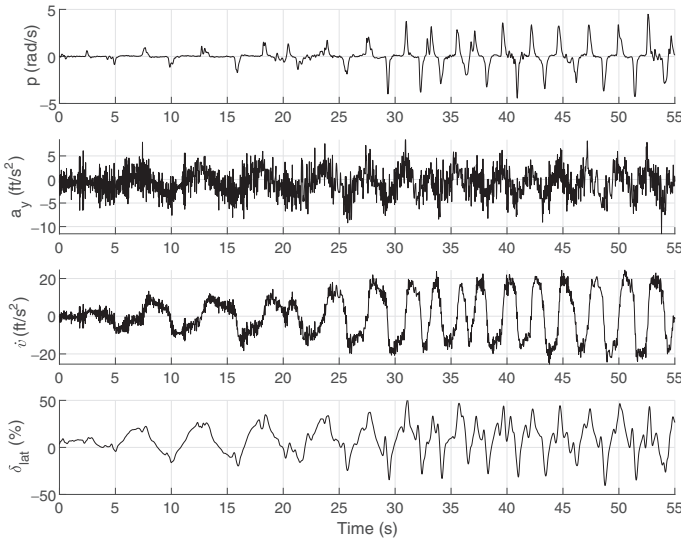Fig. 2. Quadrotor control system schematic.

Fig. 3. Frequency sweep.

The parameters to be identified are the stability derivatives Y_v, L_v, and L_p, the control derivative $L_{\delta_{\text{lat}}}$, and the time delay τ_ϕ. The lateral velocity rate $\dot{v}$, roll rate p, and lateral acceleration a_y are used as parametric identification outputs. The roll rate and lateral acceleration come, respectively, from the built-in gyro and accelerometer sensors, whereas the lateral velocity rate is reconstructed from its equation of motion at hover:

$$\dot{v} = a_y + g\phi \qquad (2)$$

The frequency sweep performed on the roll axis is shown in Fig. 3. Table 1 shows the frequency ranges adopted for each response used in the identification process. The frequency ranges are chosen such that the coherence of each response is sufficiently high across such frequency ranges. The coherence function provides a measure of the linearity of the system under test and has values between 0 and 1. Values greater than 0.6 are considered satisfactory [19]. Table 2 shows the value of the identified parameters, the Cramér–Rao (CR) bounds, and the insensitivities. The CR bounds provide a reliable measure of parameter accuracy for the frequency–response identification and indicate the level of correlation among the identification parameters [19]. Large relative CR bounds (i.e., larger than 20%) for individual parameters indicate poor identifiability and suggest that these parameters should be fixed in the model structure. Large CR bounds are typically associated with high insensitivity. High insensitivity (i.e., larger than 10%) occurs when changes in

Table 1. Frequency ranges used for the lateral dynamics identification

Response	Frequency Range (rad/s)
$\dot{v}/\delta_{\text{lat}}$	0.7–10
p/δ_{lat}	0.7–40
a_y/δ_{lat}	0.7–3

Table 2. Lateral dynamics identified parameters

Parameter	Value	CR Bound (%)	Insensitivity (%)
Y_v	−0.3022 1/s	6.107	1.825
L_v	−0.8287 rad/(ft s)	5.943	1.580
L_p	0 1/s	-	-
$L_{\delta_{\text{lat}}}$	33.514 rad/(s² %)	3.297	1.144
τ_ϕ	0.0565 s	4.170	2.077

a single parameter have a negligible effect on the fit cost, indicating that the parameter is not important in the selected model structure [19]. It should be noted that in the model structure determination phase L_p was dropped from the identification (set to 0) because of its high CR bounds. This did not negatively affect the fit cost. The average cost function associated with the identification is $J = 28$. A cost function less than $J = 50$ indicates excellent match between the identified model and the frequency responses [19]. The frequency and time domain validations of the identified model against the flight-test data are shown in Figs. 4 and 5, respectively. Overall, the identified model matches the flight data closely in both frequency and time domains.

Longitudinal dynamics

The longitudinal state-space model structure and relative output equations are, respectively,

$$\begin{bmatrix} \dot{u} \\ \dot{q} \\ \dot{\theta} \end{bmatrix} = \begin{bmatrix} X_u & 0 & -g \\ M_u & M_q & 0 \\ 0 & 1 & 0 \end{bmatrix} \begin{bmatrix} u \\ q \\ \theta \end{bmatrix} + \begin{bmatrix} 0 \\ M_{\delta_{\text{lon}}} \\ 0 \end{bmatrix} \delta_{\text{lon}}(t - \tau_\theta) \qquad (3a)$$

$$\begin{bmatrix} \dot{u} \\ q \\ a_x \end{bmatrix} = \begin{bmatrix} X_u & 0 & -g \\ 0 & 1 & 0 \\ X_u & 0 & 0 \end{bmatrix} \begin{bmatrix} u \\ q \\ \theta \end{bmatrix} \qquad (3b)$$

The parameters to be identified are the stability derivatives X_u, M_u, and M_q, the control derivative $M_{\delta_{\text{lon}}}$, and the time delay τ_θ. The longitudinal velocity rate $\dot{u}$, the pitch rate q, and the longitudinal acceleration a_x are chosen as parametric identification outputs. The pitch rate and longitudinal acceleration come, respectively, from the built-in gyro and accelerometer sensors, whereas the longitudinal velocity rate is reconstructed from its equation of motion at hover:

$$\dot{u} = a_x - g\theta \qquad (4)$$

Table 3 shows the frequency ranges adopted for each response used in the identification process. The frequency ranges are chosen such that the coherence function of each response is greater than 0.6 across such frequency ranges. Table 4 shows the value of the identified parameters, the CR bounds, and the insensitivities. It should be noted that, as for the lateral dynamics with L_p, M_q was dropped from the identification (set to 0) because of its high CR bounds. This did not negatively affect the fit cost. The average cost function associated with the identification is $J = 50$, indicating an excellent match between the identified model and the frequency responses.
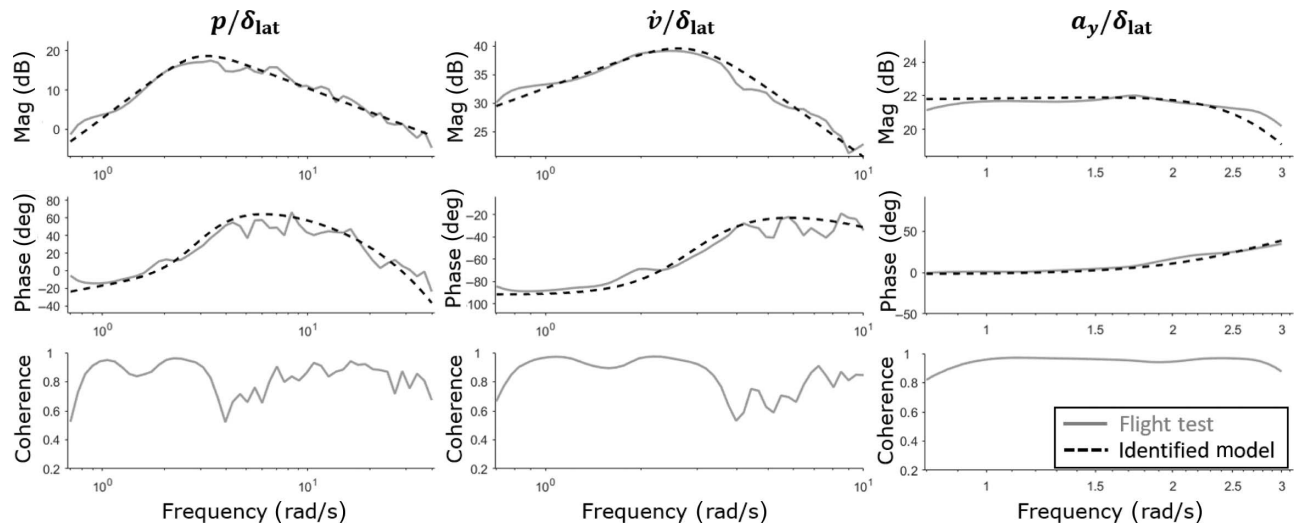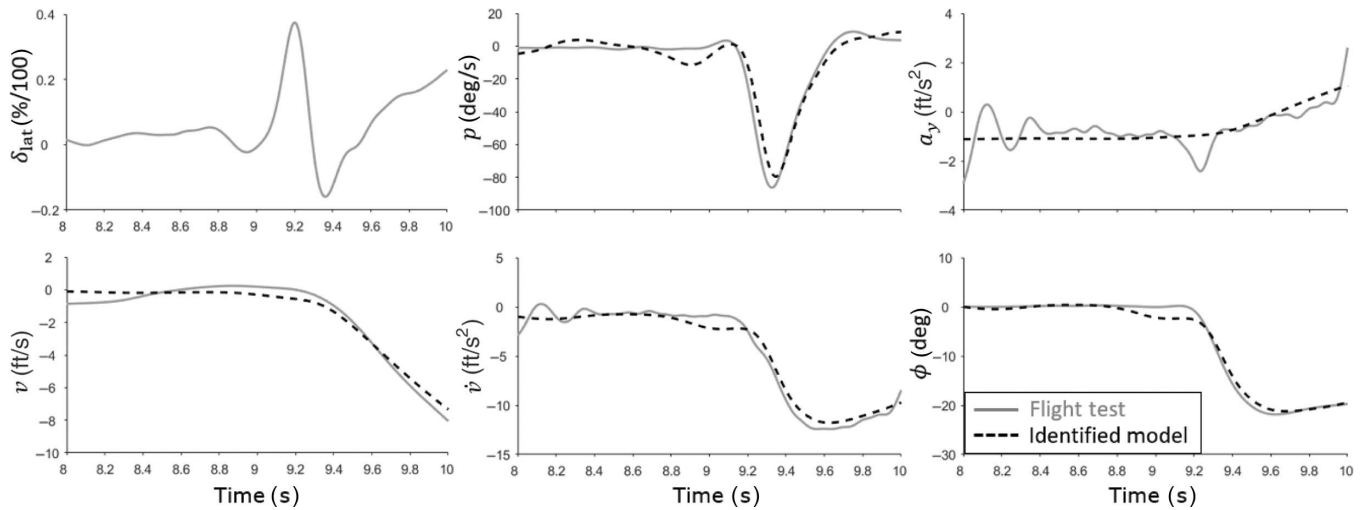
Fig. 4. Frequency domain validation.

Fig. 5. Time domain validation.

Table 3. Frequency ranges used for the lateral dynamics identification

Response	Frequency Range(rad/s)
$\dot{u}/\delta_{lon}$	0.5–10
q/δ_{lon}	0.5–30
a_x/δ_{lon}	0.5–2

Table 4. Longitudinal dynamics identified parameters

Parameter	Value	CR Bound (%)	Insensitivity (%)
X_u	-0.2568 1/s	5.302	1.814
M_u	1.1257 rad/(s ft)	5.618	1.306
M_q	0 1/s	–	–
$M_{\delta_{lon}}$	27.919 rad/(s^2 %)	4.155	1.109
τ_θ	0.0355 s	10.73	5.321

Directional dynamics

The directional state-space model structure and relative output equations are, respectively:

$$\begin{bmatrix} \dot{r} \\ \dot{\psi} \end{bmatrix} = \begin{bmatrix} N_r & 0 \\ 1 & 0 \end{bmatrix} \begin{bmatrix} r \\ \psi \end{bmatrix} + \begin{bmatrix} N_{\delta_{ped}} \\ 0 \end{bmatrix} \delta_{ped}(t - \tau_\psi) \qquad (5a)$$

$$r = [1\ 0] \begin{bmatrix} r \\ \psi \end{bmatrix} \qquad (5b)$$

The parameters to be identified are the stability derivative N_r, the control derivative $N_{\delta_{ped}}$, and the time delay τ_ψ. The yaw rate r is used as the parametric identification output. The yaw rate measurement comes from

Table 5. Frequency ranges used for the directional dynamics identification

Response	Frequency Range (rad/s)
r/δ_{ped}	0.9–11

the built-in gyro. Table 5 shows the frequency range adopted for yaw rate to lateral input response used in the identification process. The frequency range is chosen such that the coherence function of the response is greater than 0.6 across such frequency range. Table 6 shows the value of the

Table 6. Directional dynamics identified parameters

Parameter	Value	CR Bound (%)	Insensitivity (%)
N_r	-0.5617 1/s	25.19	9.713
N_{δ_ped}	6.0308 rad/(s² %)	3.877	1.848
τ_ψ	0.0401 [s]	7.023	2.452

Table 7. Frequency ranges used for the vertical dynamics identification

Response	Frequency Range (rad/s)
$\dot{w}/\delta_\text{col}$	0.4–11
$\dot{a}_z/\delta_\text{col}$	0.4–11

Table 8. Vertical dynamics identified parameters

Parameter	Value	CR Bound (%)	Insensitivity (%)
Z_w	-0.1734 1/s	39.72	16.06
Z_{δ_col}	-49.065 ft/(s² %)	2.647	1.312
τ_z	0.0389 s	30.03	12.21

Fig. 6. Eigenvalues of the identified system.

identified parameters, the CR bounds, and the insensitivities. The average cost function associated with the identification is $J = 6$, indicating an excellent match between the identified model and the frequency response.

Vertical dynamics

The vertical state-space model structure and relative output equations are, respectively,

$$\dot{w} = Z_w w + Z_{\delta_\text{col}} \delta_\text{col}(t - \tau_z) \tag{6a}$$

$$\begin{bmatrix} w \\ a_z \end{bmatrix} = \begin{bmatrix} 1 \\ Z_w \end{bmatrix} w + \begin{bmatrix} 0 \\ Z_{\delta_\text{col}} \end{bmatrix} \delta_\text{col}(t - \tau_z) \tag{6b}$$

The parameters to be identified are the stability derivative Z_w, the control derivative Z_{δ_col}, and the time delay τ_z. The vertical speed w and vertical acceleration a_z are used as parametric identification outputs. The vertical speed and the vertical acceleration come, respectively, from the the built-in estimation algorithm and gyro. Table 7 shows the frequency range adopted for the frequency responses used in the identification process. The frequency ranges are chosen such that the coherence function of the responses is greater than 0.6 across such frequency ranges. Table 8 shows the value of the identified parameters, the CR bounds, and the insensitivities. The average cost function associated with the identification is $J = 3$, indicating an excellent match between the identified model and the frequency response.

Complete state-space model

The complete state-space representation of the quadrotor rigid body dynamics is obtained by assembling the linear systems representing the dynamics around each axis. The resulting 6 DOF state space system has the following input vector, output vector, and dynamics:

$$\mathbf{x}^T = [v \ p \ \phi \ u \ q \ \theta \ r \ \psi \ w] \tag{7a}$$

$$\mathbf{u}^T = [\delta_\text{lat}(t - \tau_\phi) \ \delta_\text{lon}(t - \tau_\theta) \ \delta_\text{ped}(t - \tau_\psi) \ \delta_\text{col}(t - \tau_z)] \tag{7b}$$
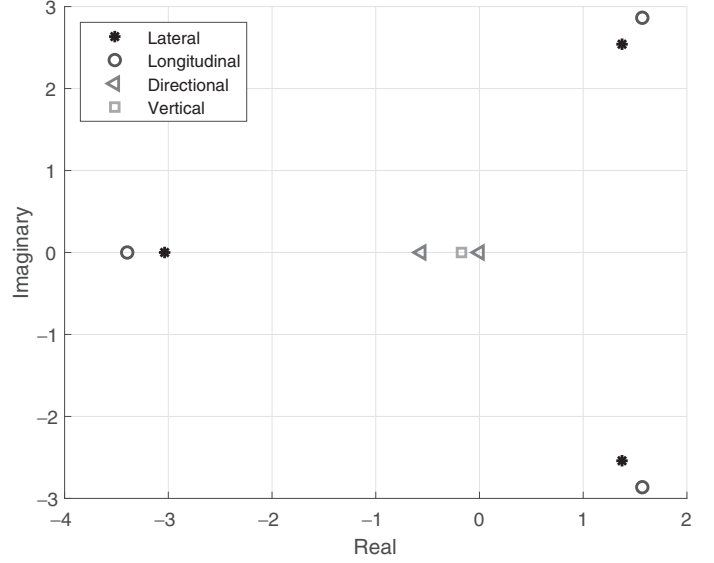
$$\mathbf{A} = \begin{bmatrix} Y_v & 0 & g & 0 & 0 & 0 & 0 & 0 & 0 \\ L_v & L_p & 0 & 0 & 0 & 0 & 0 & 0 & 0 \\ 0 & 1 & 0 & 0 & 0 & 0 & 0 & 0 & 0 \\ 0 & 0 & 0 & X_u & 0 & -g & 0 & 0 & 0 \\ 0 & 0 & 0 & M_u & M_q & 0 & 0 & 0 & 0 \\ 0 & 0 & 0 & 0 & 1 & 0 & 0 & 0 & 0 \\ 0 & 0 & 0 & 0 & 0 & 0 & N_r & 0 & 0 \\ 0 & 0 & 0 & 0 & 0 & 0 & 1 & 0 & 0 \\ 0 & 0 & 0 & 0 & 0 & 0 & 0 & 0 & Z_w \end{bmatrix},$$

$$\mathbf{B} = \begin{bmatrix} 0 & 0 & 0 & 0 \\ L_{\delta_\text{lat}} & 0 & 0 & 0 \\ 0 & 0 & 0 & 0 \\ 0 & 0 & 0 & 0 \\ 0 & M_{\delta_\text{lon}} & 0 & 0 \\ 0 & 0 & 0 & 0 \\ 0 & 0 & N_{\delta_\text{ped}} & 0 \\ 0 & 0 & 0 & 0 \\ 0 & 0 & 0 & Z_{\delta_\text{col}} \end{bmatrix} \tag{8}$$

The eigenvalues of the system are computed and reported visually in Fig. 6 and quantitatively in Table 9. The system is stable around the yaw and heave axes. The roll and pitch axes have one negative real eigenvalue and a pair of complex eigenvalues in the right half plane each, representing the classical hovering cubic dynamics present in all hovering vehicles [20]. The real negative eigenvalues are the stable roll and pitch subsidence modes. The pairs of complex eigenvalues in the right half of the plane are the unstable phugoid modes in roll and pitch. The similarity between the eigenvalues in roll and pitch are due to the symmetry of the quadrotor's configuration along both the roll and pitch axes. The slight differences may be due to the uneven distribution of the electronic components and sensors. Overall, these results are in agreement with the literature [12, 15].

Dynamic Inversion Controller

Inner loop

A DI [1,21] control law is designed to achieve stability, disturbance rejection, an attitude command/attitude hold (ACAH) response around the
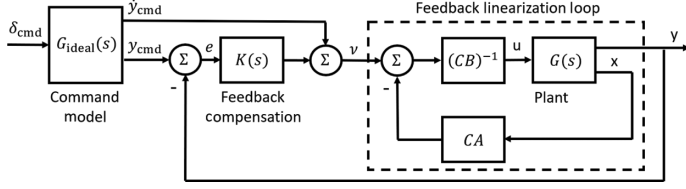
Fig. 7. DI block diagram.

Table 9. Eigenvalues of the identified system

Eigenvalue	Mode	Value
$\lambda_{1,2}$	Roll phugoid	$1.3948 \pm 2.5845i$
λ_3	Roll subsidence	-3.0919
$\lambda_{4,5}$	Pitch phugoid	$1.5698 \pm 2.8634i$
λ_6	Pitch subsidence	-3.3964
λ_7	Yaw subsidence	-0.5616
λ_8	Yaw integrator	0
λ_9	Heave subsidence	-0.1734

roll and pitch axes, and a rate command/attitude hold (RCAH) response around the yaw and heave axes. A similar controller was previously implemented on a B-430, as discussed in (Ref. 8). A general DI scheme for a Single-Input Single-Output (SISO) system is shown in Fig. 7. The key components are a command model (also known as commend model or reference model) that specifies desired response to pilot commands, a feedback compensation on the tracking error, and an inner feedback loop that achieves model inversion (also known as feedback linearization loop).

To model the DI controller, a modified state vector is defined:

$$\hat{\mathbf{x}}^T = [p\ \phi\ q\ \theta\ r\ w] \tag{9}$$

as well as modified state and control matrices:

$$\hat{\mathbf{A}} = \begin{bmatrix} L_p & 0 & 0 & 0 & 0 & 0 \\ 1 & 0 & 0 & 0 & 0 & 0 \\ 0 & 0 & M_q & 0 & 0 & 0 \\ 0 & 0 & 1 & 0 & 0 & 0 \\ 0 & 0 & 0 & 0 & N_r & 0 \\ 0 & 0 & 0 & 0 & 0 & Z_w \end{bmatrix},$$

$$\hat{\mathbf{B}} = \begin{bmatrix} L_{\delta_{\text{lat}}} & 0 & 0 & 0 \\ 0 & 0 & 0 & 0 \\ 0 & M_{\delta_{\text{lon}}} & 0 & 0 \\ 0 & 0 & 0 & 0 \\ 0 & 0 & N_{\delta_{\text{ped}}} & 0 \\ 0 & 0 & 0 & Z_{\delta_{\text{col}}} \end{bmatrix} \tag{10}$$

Given a commanded reference trajectory $\mathbf{y}_{\text{cmd}}(t)$, the interest lays in controlling the output $\mathbf{y}(t)$ so that it follows the command. In this particular application, the reference trajectory and the output are given, respectively, by Eqs. (11) and (12):

$$\mathbf{y}_{\text{cmd}}^T = [\phi_{\text{cmd}}\ \theta_{\text{cmd}}\ r_{\text{cmd}}\ V_{z\,\text{cmd}} \tag{11}$$

$$\mathbf{y}^T = [\phi\ \theta\ r\ V_z] \tag{12}$$

where ϕ, θ, and r, V_z are the roll attitude, pitch attitude, yaw rate, and vertical speed (positive up), respectively. The output matrix $\mathbf{C}$ that

Table 10. DI and EMF inner loop command models properties

Command	ω_n (rad/s)	ζ
Roll attitude	10	0.7
Pitch attitude	10	0.7
Vertical speed	1	–
Yaw rate	2	–

identifies the controlled states is given by

$$\mathbf{C} = \begin{bmatrix} \mathbf{C}_1 \\ \mathbf{C}_2 \end{bmatrix} \tag{13}$$

where

$$\mathbf{C}_1 = \begin{bmatrix} 0 & 1 & 0 & 0 & 0 & 0 \\ 0 & 0 & 0 & 1 & 0 & 0 \end{bmatrix} \tag{14a}$$

$$\mathbf{C}_2 = \begin{bmatrix} 0 & 0 & 0 & 1 & 0 \\ 0 & 0 & 0 & 0 & -1 \end{bmatrix} \tag{14b}$$

where $\mathbf{C}_1$ corresponds to the roll and pitch attitudes, whereas $\mathbf{C}_2$ is related to the yaw rate and vertical speed. This partitioning is due to the fact that the output equations for ϕ and θ have to be differentiated twice to see the controls in the output equation, while the same procedure has to be done just once for r and V_z:

$$\begin{bmatrix} \ddot{\phi} \\ \ddot{\theta} \\ \dot{r} \\ \dot{V_z} \end{bmatrix} = \begin{bmatrix} \mathbf{C}_1\hat{\mathbf{A}}^2\hat{\mathbf{x}} + \mathbf{C}_1\hat{\mathbf{A}}\hat{\mathbf{B}}\mathbf{u} \\ \mathbf{C}_2\hat{\mathbf{A}}\hat{\mathbf{x}} + \mathbf{C}_2\hat{\mathbf{B}}\mathbf{u} \end{bmatrix} \tag{15}$$

Second-order command models of the form

$$G_{\text{ideal}}(s) = \frac{\omega_n^2}{s^2 + 2\zeta\omega_n + \omega_n^2} \tag{16}$$

are used for roll and pitch attitudes, whereas first-order command models of the form

$$G_{\text{ideal}}(s) = \frac{1}{\tau s + 1} \tag{17}$$

where $\tau = 1/\omega_n$ is utilized for vertical speed and yaw rate. Table 10 shows the values used for the parameters of the command models.

Proportional integral derivative (PID) and proportional integral (PI) compensation are used to reject external disturbances and to compensate for differences between the inversion model described in the next section and the bare-airframe dynamics. The dynamic inversion control law is thus given by

$$\mathbf{u} = \begin{bmatrix} \mathbf{C}_1\hat{\mathbf{A}}\hat{\mathbf{B}} \\ \mathbf{C}_2\hat{\mathbf{B}} \end{bmatrix}^{-1} \left(\mathbf{\nu} - \begin{bmatrix} \mathbf{C}_1\hat{\mathbf{A}}^2 \\ \mathbf{C}_2\hat{\mathbf{A}} \end{bmatrix}\hat{\mathbf{x}} \right) \tag{18}$$

where ν is the pseudocommand vector and e is the error as given, respectively, in Eqs. (19) and (20).

$$\begin{bmatrix} \nu_\phi \\ \nu_\theta \\ \nu_r \\ \nu_{V_z} \end{bmatrix} = \begin{bmatrix} \ddot{\phi}_{\text{cmd}} \\ \ddot{\theta}_{\text{cmd}} \\ \dot{r}_{\text{cmd}} \\ \dot{V}_{z\,\text{cmd}} \end{bmatrix} + \mathbf{K}_P\begin{bmatrix} e_\phi \\ e_\theta \\ e_r \\ e_{V_z} \end{bmatrix} + \mathbf{K}_D\begin{bmatrix} \dot{e}_\phi \\ \dot{e}_\theta \\ 0 \\ 0 \end{bmatrix} + \mathbf{K}_I\begin{bmatrix} \int e_\phi dt \\ \int e_\theta dt \\ \int e_r dt \\ \int e_{V_z} dt \end{bmatrix} \tag{19}$$

$$\mathbf{e} = \mathbf{y}_{\text{cmd}} - \mathbf{y}; \tag{20}$$

where $\mathbf{K}_P$, $\mathbf{K}_D$, and $\mathbf{K}_I$ are 4×4 diagonal matrices identifying, respectively, the proportional, derivative, and integral gain matrices. A DI inner loop block diagram is shown in Fig. 8.
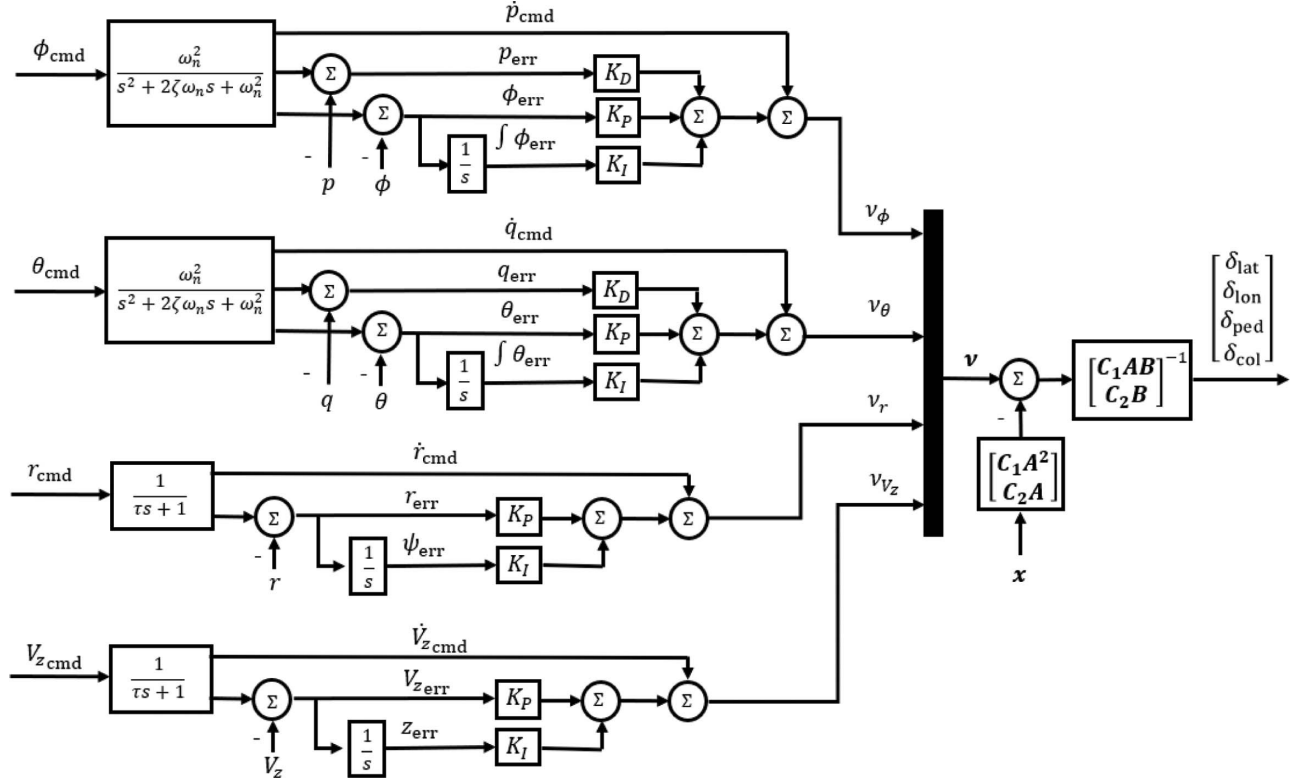
Fig. 8. DI inner loop.

Table 11. Outer loop command models properties

	τ(s)
$V_{x_{cmd}}$	1
$V_{y_{cmd}}$	1

Outer loop

The outer loop controller tracks forward and lateral ground velocities in the heading frame. The heading frame is a vehicle carried frame, where the x-axis is aligned with the current aircraft heading, the z-axis is positive up in the inertial frame, and the y-axis points to the right, forming a left-handed orthogonal coordinate system. Equation (21 shows the rotation from body to the heading frame:

$$\mathbf{T}_{h/b} = \begin{bmatrix} \cos\theta & \sin\phi\sin\theta & \cos\phi\sin\theta \\ 0 & \cos\phi & -\sin\phi \\ \sin\theta & -\sin\phi\cos\theta & -\cos\phi\cos\theta \end{bmatrix} \quad (21)$$

such that the velocities in the heading frame are given by

$$\begin{bmatrix} V_x \\ V_y \\ V_z \end{bmatrix} = \mathbf{T}_{h/b} \begin{bmatrix} u \\ v \\ w \end{bmatrix} \quad (22)$$

The command models for both lateral and forward velocities, V_x and V_y, are first order. The time constants are given in Table 11. The filtered velocities are subtracted from their measurements to find the error, which goes through a PI controller. The feed-forward signal is subsequently

added, leading to the desired commands:

$$\begin{bmatrix} \nu_{V_x} \\ \nu_{V_y} \end{bmatrix} = \begin{bmatrix} \dot{V}_{x_{cmd}} \\ \dot{V}_{y_{cmd}} \end{bmatrix} + \mathbf{K}_P \begin{bmatrix} e_{V_x} \\ e_{V_y} \end{bmatrix} + \mathbf{K}_I \begin{bmatrix} \int e_{V_x} dt \\ \int e_{V_y} dt \end{bmatrix} \quad (23)$$

Lateral velocity is controlled by commanding roll angle. Consider the lateral velocity equation of motion:

$$\dot{V}_y = Y_v V_y + g\phi_{cmd} \quad (24)$$

DI is applied, leading to the following inverse law:

$$\phi_{cmd} = \frac{1}{g}(\nu_{V_y} - Y_v V_y) \quad (25)$$

Similarly, longitudinal velocity is controlled by commanding pitch angle. Consider the longitudinal velocity equation of motion:

$$\dot{V}_x = X_u V_x - g\theta_{cmd} \quad (26)$$

DI is applied, leading to the following inverse law:

$$\theta_{cmd} = -\frac{1}{g}(\nu_{V_x} - X_u V_x) \quad (27)$$

A DI outer loop block diagram is shown in Fig. 9.

Error dynamics

Feedback compensation is needed both in the inner and the outer loops for two main reasons. First, we use approximations and the inversion is not exact. Second, there are external disturbances to the system. It can be demonstrated [21] that for a DI controller the output equation must be differentiated n times for the controls to to appear explicitly in the
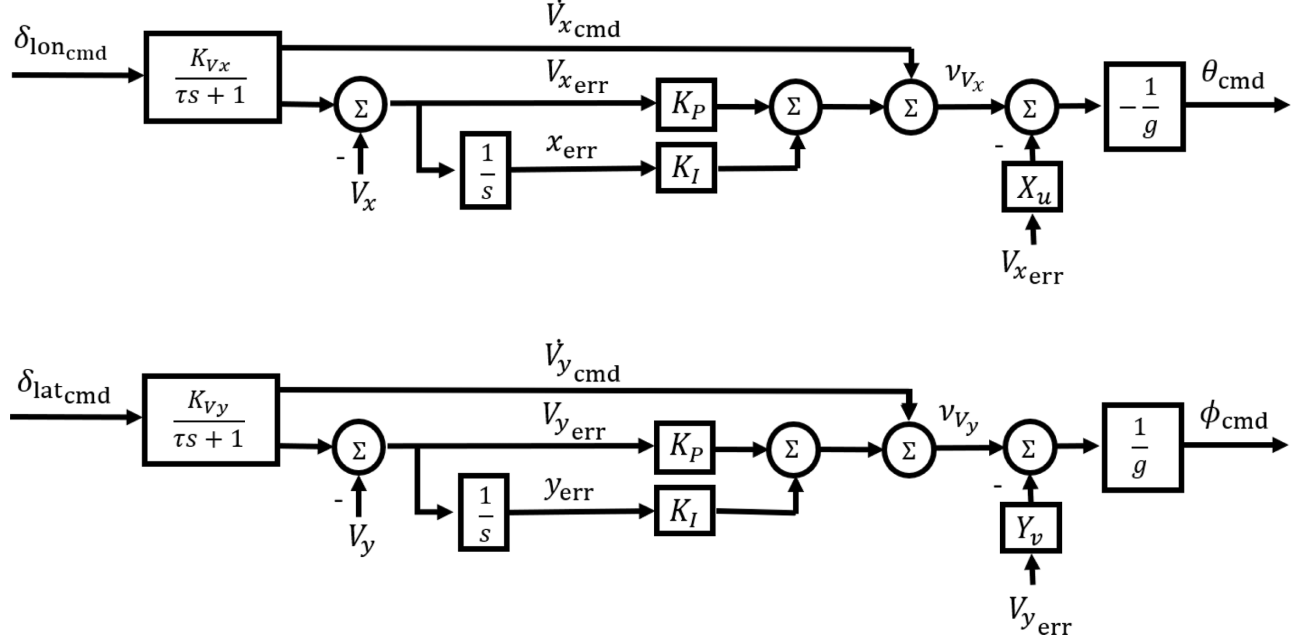
Fig. 9. DI outer loop.

output equation:

$$e^{(n)} = y_{\text{cmd}}^{(n)} - \nu \tag{28}$$

For the states for which this has to be done twice, a PID control strategy applied to the pseudocommand vector is given by

$$\nu = \ddot{y}_{\text{cmd}}(t) + K_D \dot{e}(t) + K_P e(t) + K_I \int_0^t e(\tau)d\tau \tag{29}$$

By substituting Eq. (29) into Eq. (28), the closed-loop error dynamics is obtained:

$$\ddot{e}(t) + K_D \dot{e}(t) + K_P e(t) + K_I \int_0^t e(\tau)d\tau = 0 \tag{30}$$

The gains can be chosen so that the frequencies of the error dynamics are of the same order as the command models, ensuring that the bandwidth of the response to disturbances is comparable to the one of an input given by a pilot or outer loop. By taking the Laplace transform and therefore switching to frequency domain, the error dynamics becomes

$$e(s)\left(s^2 + K_D s + K_P + \frac{1}{s}K_I\right) = 0 \tag{31}$$

or equivalently

$$e(s)(s^3 + K_D s^2 + K_P s + K_I) = 0 \tag{32}$$

To obtain gains that would guarantee a desired response, the error dynamics can be set equal to the third-order system given in Eq. (33):

$$(s^2 + 2\zeta\omega_n s + \omega_n^2)(s + p) = 0 \tag{33}$$

Developing the product between the polynomials leads to

$$s^3 + (p + 2\zeta\omega_n)s^2 + (2\zeta\omega_n p + \omega_n^2)s + \omega_n^2 p = 0 \tag{34}$$

Setting the coefficients of the polynomial equal to the the gains of Eq. (32) results in

$$K_D = 2\zeta\omega_n + p \tag{35a}$$
$$K_P = 2\zeta\omega_n p + \omega_n^2 \tag{35b}$$
$$K_I = \omega_n^2 p \tag{35c}$$

Specifically, this approach is used for ϕ and θ in the inner loop.

Similarly, for those states for which PI compensation is applied, the pseudocommand vector is given by

$$\nu = \dot{y}_{\text{cmd}}(t) + K_P e(t) + K_I \int_0^t e(\tau)d\tau \tag{36}$$

which leads to the following closed-loop error dynamics:

$$\dot{e}(t) + K_P e(t) + K_I \int_0^t e(\tau)d\tau = 0 \tag{37}$$

and, therefore, to

$$s + K_P + \frac{1}{s}K_I = 0 \tag{38}$$

The resulting gains are

$$K_P = 2\zeta\omega_n \tag{39a}$$
$$K_I = \omega_n^2 \tag{39b}$$

This type of compensation is applied to V_z and r in the inner loop and to V_x and V_y in the outer loop. Tables 12 and 13 show the natural frequencies, damping ratios, time constants, and the integrator pole values, respectively, for the inner and the outer loops. Note that the integrator pole p is usually chosen to be one-fifth of the natural frequency, corresponding to about one-fifth of the loop crossover frequency [11]. Further, the outer loop error dynamics natural frequency must be 1/10–1/5 of the inner loop error dynamics natural frequency to ensure sufficient frequency separation [11]. The numerical value of the resulting gains is shown in Tables 14 and 15.

Table 12. DI inner loop disturbance rejection frequencies, damping ratios, and integrator poles

	ω_n(rad/s)	ζ	p
ϕ_{cmd}	10	0.7	2
θ_{cmd}	10	0.7	2
r_{cmd}	1	0.7	–
$V_{z_{cmd}}$	1	0.7	–

Table 13. DI outer loop disturbance rejection frequencies and damping ratios

	ω_n(rad/s)	ζ
$V_{x_{cmd}}$	1	0.7
$V_{y_{cmd}}$	1	0.7

Table 14. DI inner loop compensation gains

	K_D	K_P	K_I
ϕ_{cmd}	16	128	200
θ_{cmd}	16	128	200
r_{cmd}	–	1.4	1
$V_{z_{cmd}}$	–	0.3	0.5

Table 15. Outer loop compensation gains

	K_P	K_I
$V_{x_{cmd}}$	1.4	1
$V_{y_{cmd}}$	1.4	1

Explicit Model Following Controller

Inner loop

An EMF control law is designed to achieve stability, disturbance rejection, ACAH response around the roll and pitch axes, and RCAH response around the yaw and heave axes. A general EMF scheme for a SISO system is shown in Fig. 10. The inverse plant is based on a set of decoupled first- and second-order linear models, where the stability and control derivatives are taken from the identified model. Specifically, the inverse plant on the roll, pitch, and yaw axes is approximated,

respectively, by the following inverse transfer functions:

$$\frac{\delta_{lat}}{\phi} = \frac{s(s - L_p)}{L_{\delta_{lat}}} \tag{40a}$$

$$\frac{\delta_{lon}}{\theta} = \frac{s(s - M_q)}{M_{\delta_{lon}}} \tag{40b}$$

$$\frac{\delta_{ped}}{r} = \frac{s - N_r}{N_{\delta_{ped}}} \tag{40c}$$

$$\frac{\delta_{col}}{V_z} = \frac{s - Z_w}{Z_{\delta_{col}}} \tag{40d}$$

The equivalent time delays that are used to delay the ideal response on each axis are the identified time delays τ_ϕ, τ_θ, τ_ψ, and τ_z. LQRF is used for stability and disturbance rejection. The modified state vector and dynamics used to obtain the Linear Quadratic Regulator (LQR) gains is

$$\hat{\mathbf{x}}^T = [p\ \phi\ \int \phi\ q\ \theta\ \int \theta\ r\ \int r\ V_z\ z] \tag{41}$$

$$\hat{\mathbf{A}} = \begin{bmatrix} L_v & L_p & 0 & 0 & 0 & 0 & 0 & 0 & 0 & 0 \\ 0 & 1 & 0 & 0 & 0 & 0 & 0 & 0 & 0 & 0 \\ 0 & 0 & 1 & 0 & 0 & 0 & 0 & 0 & 0 & 0 \\ 0 & 0 & 0 & M_u & M_q & 0 & 0 & 0 & 0 & 0 \\ 0 & 0 & 0 & 0 & 1 & 0 & 0 & 0 & 0 & 0 \\ 0 & 0 & 0 & 0 & 0 & 1 & 0 & 0 & 0 & 0 \\ 0 & 0 & 0 & 0 & 0 & 0 & N_r & 0 & 0 & 0 \\ 0 & 0 & 0 & 0 & 0 & 0 & 1 & 0 & 0 & 0 \\ 0 & 0 & 0 & 0 & 0 & 0 & 0 & 0 & Z_w & 0 \\ 0 & 0 & 0 & 0 & 0 & 0 & 0 & 0 & 1 & 0 \end{bmatrix},$$

$$\hat{\mathbf{B}} = \begin{bmatrix} L_{\delta_{lat}} & 0 & 0 & 0 \\ 0 & 0 & 0 & 0 \\ 0 & 0 & 0 & 0 \\ 0 & M_{\delta_{lon}} & 0 & 0 \\ 0 & 0 & 0 & 0 \\ 0 & 0 & 0 & 0 \\ 0 & 0 & N_{\delta_{ped}} & 0 \\ 0 & 0 & 0 & 0 \\ 0 & 0 & 0 & Z_{\delta_{col}} \\ 0 & 0 & 0 & 0 \end{bmatrix} \tag{42}$$

Note that integrators have been added for the roll and pitch attitude and yaw rate. An EMF inner loop block diagram is shown in Fig. 11.

Outer loop

The EMF outer loop controller tracks forward and lateral velocities in the heading frame. The command models are first order and share the same time constants as the DI command models. The inverse plant is
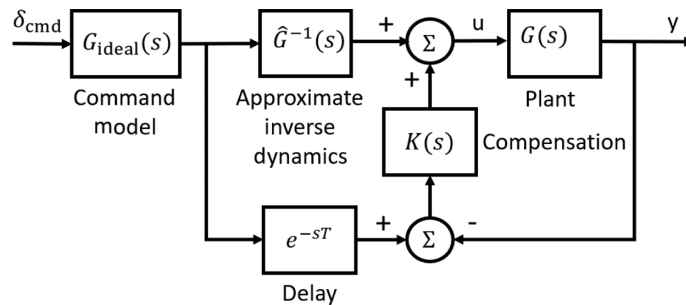
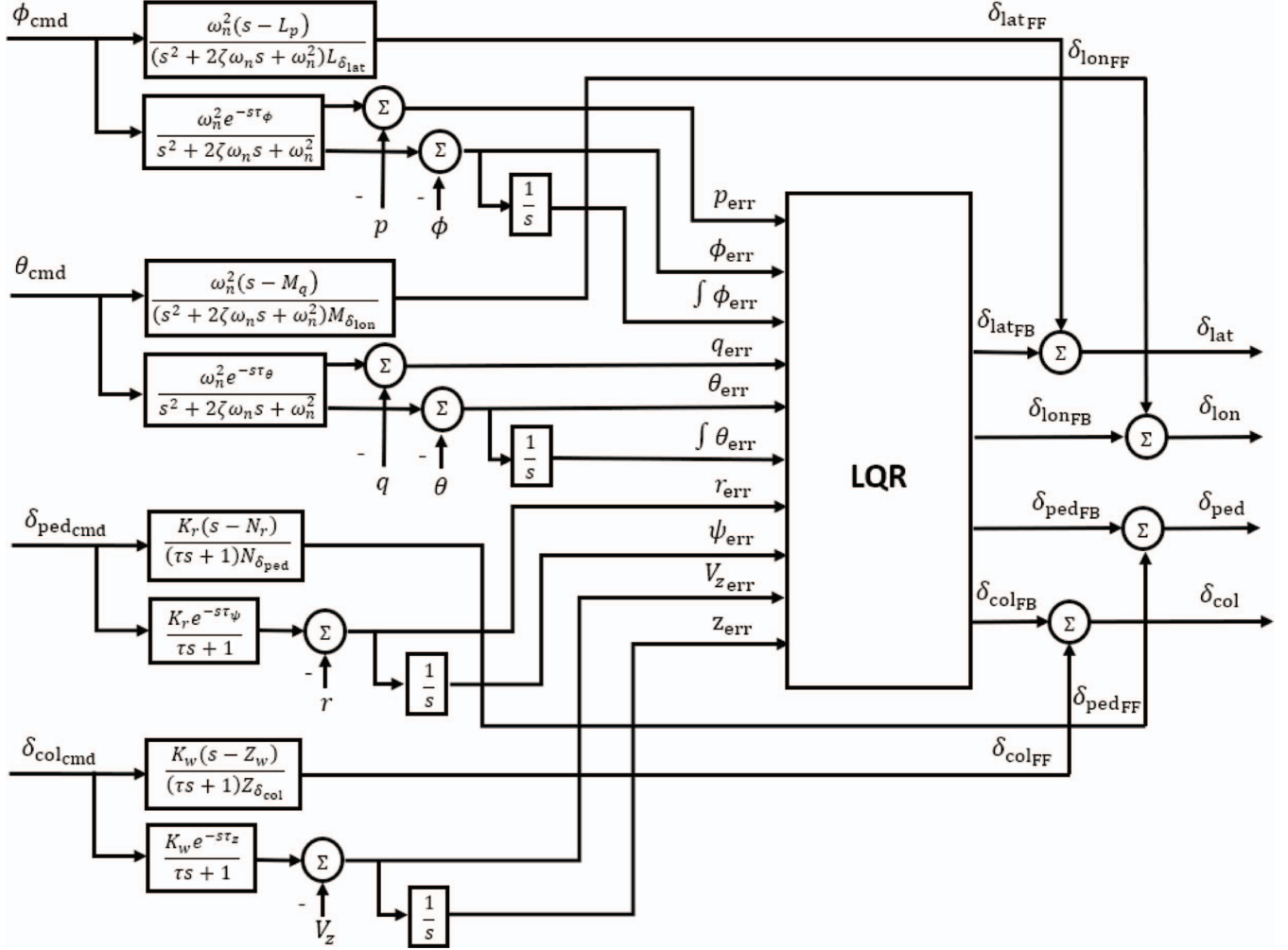**Fig. 10. EMF block diagram.**

Fig. 11. EMF inner loop.

approximated by the following first-order inverse transfer functions:

$$\frac{\theta_{\text{cmd}}}{V_x} = \frac{s - X_u}{-g} \tag{43a}$$

$$\frac{\phi_{\text{cmd}}}{V_y} = \frac{s - Y_v}{g} \tag{43b}$$

These approximate models match the bare-airframe dynamics at low frequency. LQR is used independently on each axis for disturbance rejection. The system used to synthesize the gains for the forward speed is

$$\begin{bmatrix} \dot{V}_x \\ \dot{x} \end{bmatrix} = \begin{bmatrix} X_u & 0 \\ 1 & 0 \end{bmatrix} \begin{bmatrix} V_x \\ x \end{bmatrix} + \begin{bmatrix} -g \\ 0 \end{bmatrix} \theta_{\text{cmd}} \tag{44}$$

where x is the longitudinal position in the heading frame. The system used to synthesize the gains for the lateral speed is

$$\begin{bmatrix} \dot{V}_y \\ \dot{y} \end{bmatrix} = \begin{bmatrix} Y_v & 0 \\ 1 & 0 \end{bmatrix} \begin{bmatrix} V_y \\ y \end{bmatrix} + \begin{bmatrix} g \\ 0 \end{bmatrix} \phi_{\text{cmd}} \tag{45}$$

where y is the lateral position in the heading frame. An EMF outer loop block diagram is shown in Fig. 12.

Disturbance rejection

Since the feedback loop that acts on the error dynamics from the commanded states of Fig. 10 is independent from the the inverse plant, the LQR gains for both inner and outer loop can be determined from the models discussed in the previous sections. The cost function being minimized is

$$J = \int_0^t [\hat{\mathbf{x}}^T \mathbf{Q} \hat{\mathbf{x}} + \mathbf{u}^T \mathbf{R} \mathbf{u}] d\tau \tag{46}$$

The weighting matrices are designed according to Bryson's rule [22]:

$$\mathbf{Q} = \text{diag}\left[\frac{\alpha_1^2}{(x_1)_{\text{max}}^2} \quad \cdots \quad \frac{\alpha_n^2}{(x_l)_{\text{max}}^2} \right] \tag{47}$$

$$\mathbf{R} = \rho \, \text{diag}\left[\frac{\beta_1^2}{(u_1)_{\text{max}}^2} \quad \cdots \quad \frac{\beta_m^2}{(u_m)_{\text{max}}^2} \right] \tag{48}$$

where $(x_i)_{\text{max}}^2$ and $(u_j)_{\text{max}}^2$ are the largest desired response and input for that particular component of the output/input, $\sum_{i=1}^l \alpha_i^2 = 1$ and $\sum_{j=1}^m \beta_i^2 = 1$ are used to add an additional relative weighting on the various components of the output/control input, and ρ is used as the relative weighting between the control and state penalties. Tables 16 and 17 show the penalties on the states and controls used in the inner loop
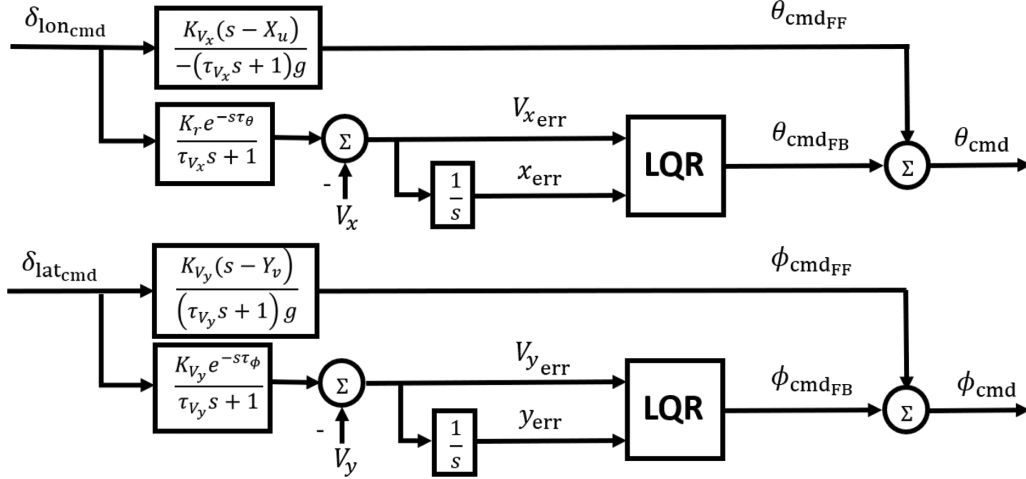
Fig. 12. EMF outer loop.

Table 16. EMF inner loop LQR state penalties

	$(x_i)_{max}$	α_i^2
p	$\pi/180$	1/10
ϕ	$\pi/180$	1/10
$\int \phi$	$0.05\pi/180$	1/10
q	$\pi/180$	1/10
θ	$\pi/180$	1/10
$\int \theta$	$0.05\pi/180$	1/10
r	$\pi/180$	1/10
$\int r$	$\pi/180$	1/10
V_z	1	1/10
z	1	1/10

Table 17. EMF inner loop LQR control penalties

	$(u_i)_{max}$	β_i^2
δ_{lat}	0.01	1/4
δ_{lon}	0.01	1/4
δ_{ped}	0.01	1/4
δ_{col}	0.01	1/4

Table 18. EMF outer loop LQR state penalties

	$(x_i)_{max}$	α_i^2
V_x	1	1/2
x	1	1/2
V_y	1	1/2
y	1	1/2

Table 19. EMF outer loop LQR control penalties

	$(u_i)_{max}$	β_i^2
θ_{cmd}	$\pi/180$	1
ϕ_{cmd}	$\pi/180$	1

subsequently, first the inner loop then the outer loop, to achieve desired performance levels.

Unscented Approach to Stability and Performance Robustness Analyses

Stability and performance robustness analyses of the DI and EMF controllers are performed by perturbing the identified stability and control derivatives of the bare-airframe and evaluating stability margins, disturbance rejection bandwidth (DRB), and disturbance rejection peak (DRP) [23]. Essentially, it is desired to evaluate the statistics (mean and variance) of the controller performance based on the known statistics of the identified parameters. To do this robustness analysis in an efficient manner, as opposed to Monte Carlo dispersions, an unscented transform [18] is used as explained for the roll axis below. The unscented transform approach is chosen because it requires fewer data points than Monte Carlo.

To perform the unscented transform, the covariance matrix **P** for the vector of identified parameters Θ is needed. The covariance matrix is calculated from the CIFER® identification results as

$$\mathbf{P} = \mathscr{H}^{-1} \tag{49}$$

where $\mathscr{H}$ is the parameter identification Hessian matrix [19]. The Hessian matrix is composed by the second-order partial derivatives of the identification fit cost J with respect to the identified parameters vector Θ:

$$\mathscr{H} = \frac{\partial^2 J}{\partial \Theta \partial \Theta^T} \tag{50}$$

The CR bound of the ith identified parameter of the identified parameters vector is related to the Hessian matrix in the following way:

$$CR_i = \sqrt{(\mathscr{H}^{-1})_{ii}} \tag{51}$$

LQR design, where $\rho = 2$. Tables 18 and 19 show the penalties on the states and controls used in the outer loop LQR design, where $\rho = 0.25$ for both lateral and longitudinal axes. The penalties relative to the position and linear velocities states are set to 1 m/s. The penalties relative to the angular states are set to the equivalent of 1 deg ($\pi/180$ rad), with the exception of the penalties of integral of the attitude tracking error; these are found to require a significantly lower value than the equivalent of 1 deg. The penalties relative to the controls are set to the 1% (or 0.01). The relative weightings in the inner and outer loops are adjusted

Table 20. Sigma points

	$x^{(1)}$	$x^{(2)}$	$x^{(3)}$	$x^{(4)}$	$x^{(5)}$	$x^{(6)}$
Y_v	−0.3120	−0.2619	−0.3064	−0.2675	−0.2829	−0.2910
L_v	−0.8066	−0.7677	−0.8608	−0.7134	−0.8255	−0.7488
$L_{\delta_{\text{lat}}}$	33.2606	33.2525	33.2182	33.2949	31.3432	35.1698

It should be noted that the CR bounds are best expressed as a percentage of the nominal identification values:

$$\overline{\text{CR}}_i = \left| \frac{\text{CR}_i}{\Theta_i} \right| \times 100\% \tag{52}$$

The next step in performing the unscented transform is determining the sigma points $\mathbf{x}^{(i)}$ that will be used as the perturbed parameters:

$$\mathbf{x}^{(i)} = \bar{\mathbf{x}} + \tilde{\mathbf{x}}^{(i)}, \quad i = 1, ..., 2n \tag{53}$$

where

$\bar{\mathbf{x}} = \Theta$ is a vector of the nominal identified stability and control derivative values,

n is the number of identified parameters being perturbed,

$\tilde{\mathbf{x}}^{(i)} = +(\sqrt{n\mathbf{P}})_i^T$ for $i = 1, ..., n$

$\tilde{\mathbf{x}}^{(i+n)} = -(\sqrt{n\mathbf{P}})_i^T$ for $i = 1, ..., n$, and

$(\sqrt{n\mathbf{P}})_i^T$ corresponds to the ith row of the matrix $(\sqrt{n\mathbf{P}})$.

The perturbed values of the stability and control derivatives, given by the sigma points $\mathbf{x}^{(i)}$, are then used to evaluate the stability margins and disturbance rejection characteristics (DRB and DRP) of the controllers. This becomes the nonlinear transform of the sigma points $\mathbf{x}^{(i)}$, with the outputs being gain and phase margins, DRB, and DRP. Note that through this unscented transform, only $2n$ evaluations are done to assess the robustness of the controller through the statistics of the stability margins, DRB, and DRP. Once the $2n$ values of gain and phase margins, DRB, and DRP are computed, they are used to draw 1σ, 2σ, and 3σ confidence ellipsoids on the specifications. It should also be noted that the confidence ellipsoids only represent a Gaussian approximation of the propagated model uncertainty. This is because when a Gaussian distribution is propagated through a nonlinear system through an unscented transform, the resulting distribution is no longer Gaussian [18].

A stability and performance robustness analysis of the DI and EMF controllers is performed by perturbing the identified stability and control derivatives relative to the lateral dynamics. The vector of the nominal identified parameters is

$$\bar{\mathbf{x}}^T = [Y_v \ L_v \ L_{\delta_{\text{lat}}}] \tag{54}$$

The covariance matrix relative to the identified lateral dynamics is

$$\mathbf{P} = \begin{bmatrix} 0.0003 & 0.0006 & -0.0024 \\ 0.0006 & 0.0024 & 0.0254 \\ -0.0024 & 0.0254 & 1.2207 \end{bmatrix} \tag{55}$$

Since the uncertain parameter in this analysis is $n = 3$, the number of sigma points is $2n = 6$. The sigma points calculated according to Eq. (53) are reported in Table 20. These sigma points are used to evaluate the stability margins and disturbance rejection characteristics (DRB and DRP) of the DI and EMF controllers. The results are presented in the next section.

Results

Time domain

Batch simulations are run to test and compare the EMF and DI controllers. The gains are adjusted such that the two control strategies give
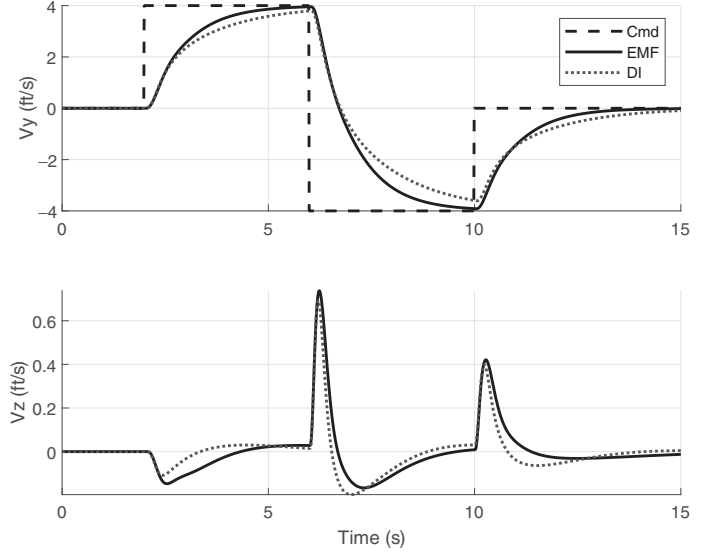
Fig. 13. Heading frame velocities time response.
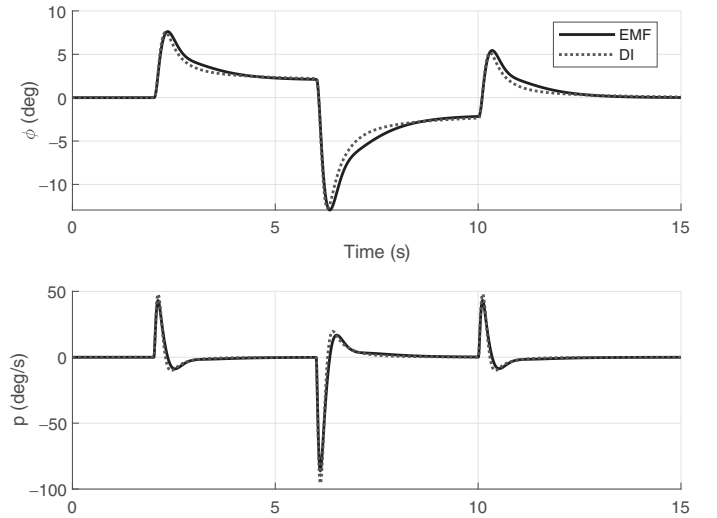
Fig. 14. Angular rates time response.

similar performances. The results shown in this section refer to a lateral speed command doublet. Figure 13 shows the heading frame velocities. Figure 14 shows the angular rates and the attitude response. Figure 15 shows the controls time history. EMF and DI show an outstanding agreement both in the on-axis and off-axis response.

Frequency domain

Inner loop. Figure 16 shows the inner attitude loop broken-loop response (loop broken at the input to the mixer) for both the DI and EMF controllers. Table 21 shows the inner attitude loop crossover frequencies and gain and phase margins of both the DI and EMF controllers. Both loops have similar crossover frequencies ω_{c_ϕ} by design. The inner loops were designed with a reduced phase margin requirement of (Phase Margin) PM ≥ 35 deg. The EMF design meets this requirement with PM $= 40.3$ deg, whereas the DI design nearly meets the requirement with PM $= 34.4$ deg. Both designs meet the nominal gain margin requirement of (Gain Margin) GM ≥ 6 dB. Figure 17 shows the attitude disturbance response
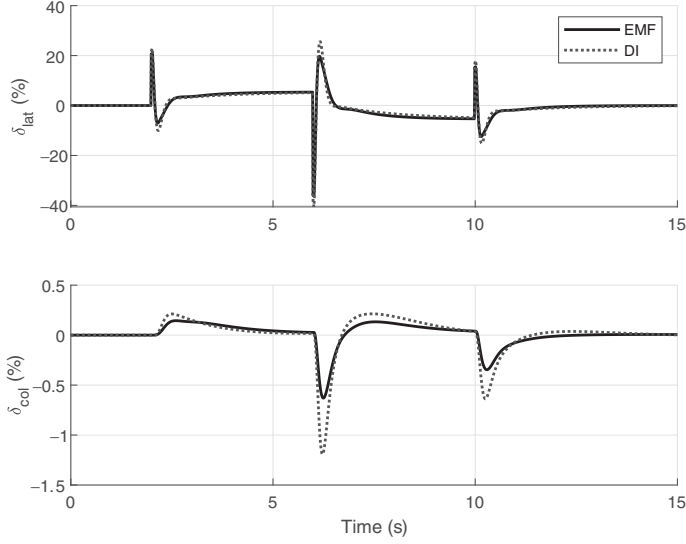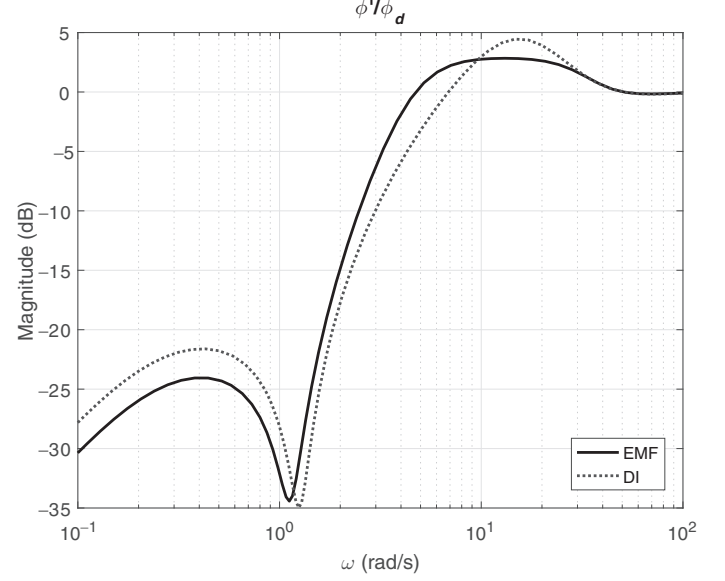
Fig. 15. Controls time response.

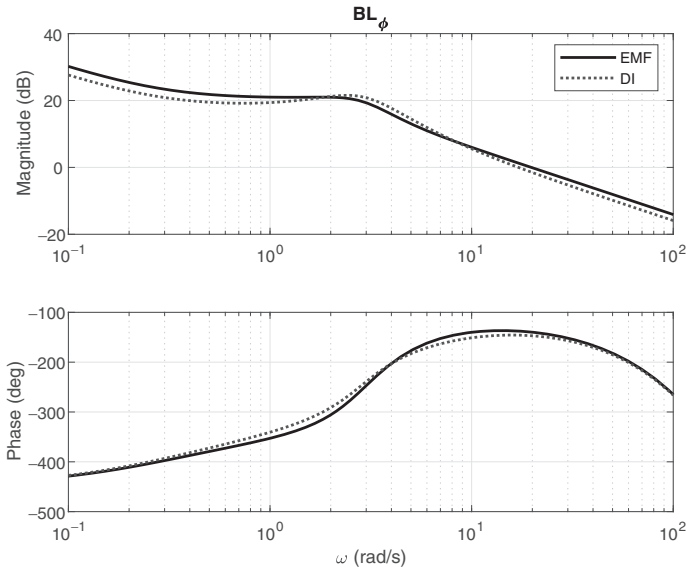Fig. 16. Inner-loop broken-loop response (loop broke at input to mixer).
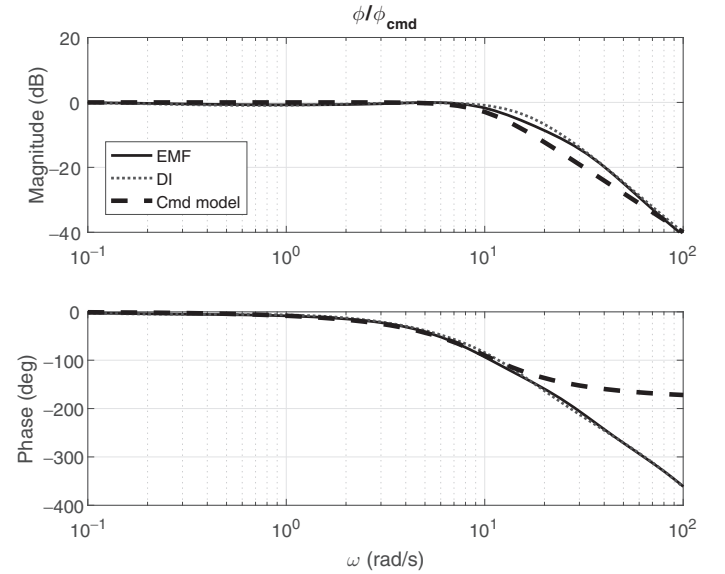

Fig. 17. Attitude disturbance response.

Fig. 18. Attitude command closed-loop response.

for both the DI and EMF controllers. Table 22 lists the attitude distur-bance rejection bandwidth (DRB) and peak (DRP) [23] values for the two controllers. The DI controller has a higher DRB and DRP than the EMF controller. This demonstrates Bode's integral theorem [24] between the two controllers, where a reduction in magnitude in one frequency range of the sensitivity function comes at the cost of an increase in magnitude at another frequency range. Figure 18 shows the closed-loop attitude response of the two controllers as compared to their common command model. Both designs have excellent model tracking performance across a wide frequency range. In addition, the closed-loop attitude response of both controllers is lower order, validating the simple inverse model designs used for the outer loop of each design.

Outer loop. Figure 19 shows the outer velocity loop broken-loop re-sponse (loop broken at the input to the inner loop) for both the DI and

EMF controllers, and Table 21 lists the outer velocity loop crossover frequencies and gain and phase margins. Note that by design, the outer-loop crossover frequencies are about $\omega_{c_v} \approx \omega_{c_\phi}/10$, to have good fre-quency separation between the inner and outer loops. Furthermore, the outer loops of both DI and EMF designs have sufficient gain and phase margins. Figure 20 shows the velocity disturbance response for both the DI and EMF controllers. Table 22 lists the velocity DRB and DRP values for the two controllers. Both controllers have similar values for velocity DRB and DRP. Finally, Fig. 21 shows the closed-loop velocity response to velocity command. Both controllers have similar closed-loop responses and excellent model following performance. These results show that the DI and EMF controllers, designed with different methods but to meet the same specifications, produce very similar results. Both designs will be taken to flight to assess their performance.
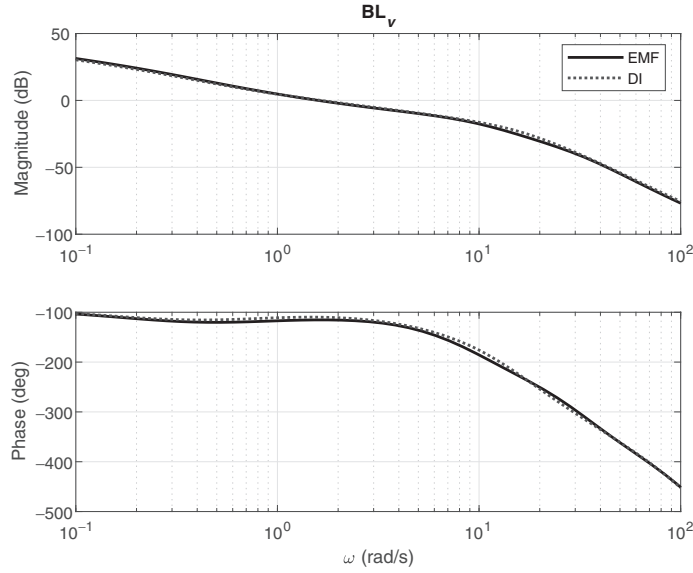
Fig. 19. Outer-loop broken-loop response (loop broke at input to inner-loop).

Fig. 20. Velocity disturbance response.

Table 21. Lateral axis broken loop gain and phase margins

	ω_c (rad/s)	GM (dB)	PM (deg)
$BL_{\phi_{DI}}$	17.8	9.22	34.3
$BL_{\phi_{EMF}}$	20.4	7.8	40.3
$BL_{v_{DI}}$	1.59	18.4	66.8
$BL_{v_{EMF}}$	1.6	21.5	67.4

Table 22. Lateral axis disturbance response gain and phase margins

	DRB (rad/s)	DRP (dB)
$\phi'/\phi_{d_{DI}}$	5.12	4.45
$\phi'/\phi_{d_{EMF}}$	3.69	2.83
$v'/v_{d_{DI}}$	1.77	1.89
$v'/v_{d_{EMF}}$	1.24	1.59

Fig. 21. Velocity command closed-loop response.

Stability and performance robustness analyses

Inner loop. Figure 22 shows the inner attitude loop stability margin robustness for both the EMF and DI controllers. The confidence ellipsoids are flat (appearing as lines), with gain and phase margin varying together with perturbations to the stability and control derivatives. This is because the inner loop crossover frequency is around $\omega_c = 20$ rad/s, while the perturbed stability and control derivatives affect the rigid body dynamics of the quadrotor (namely the lateral hovering cubic) at a much lower frequency. At high frequency (around $\omega = 20$ rad/s), these effects are seen as a pure gain shift. Furthermore, since both DI and EMF controllers inner attitude broken-loop response BL_ϕ phase curve is flat around crossover frequency (Fig. 16), a gain shift in the broken-loop response has a larger effect on the gain margin than the phase margin, as seen by the orientation of the DI and EMF confidence ellipsoids in Fig. 22. The DI confidence ellipsoids lie along the Level 1/Level 2 boundary, staying within about 2 deg of the boundary. For the EMF controller, a change in the gain of the broken-loop response affects both the gain and the phase margin. However, as seen in Fig. 22, the confidence ellipsoids for the EMF controller
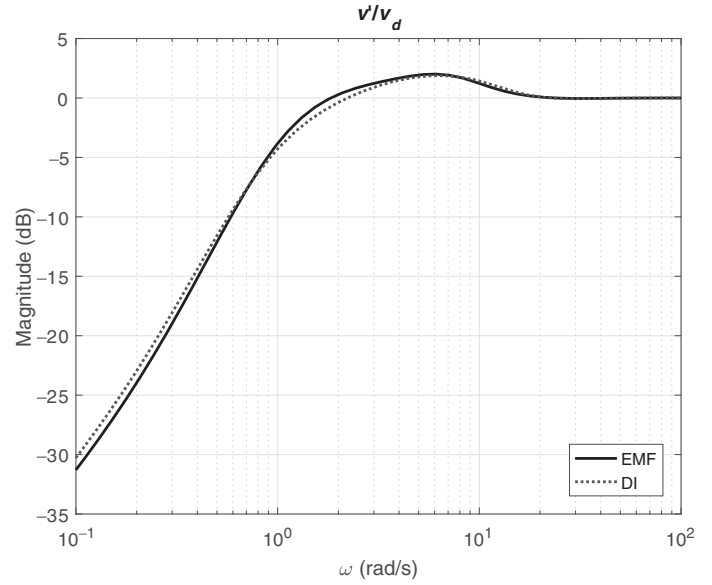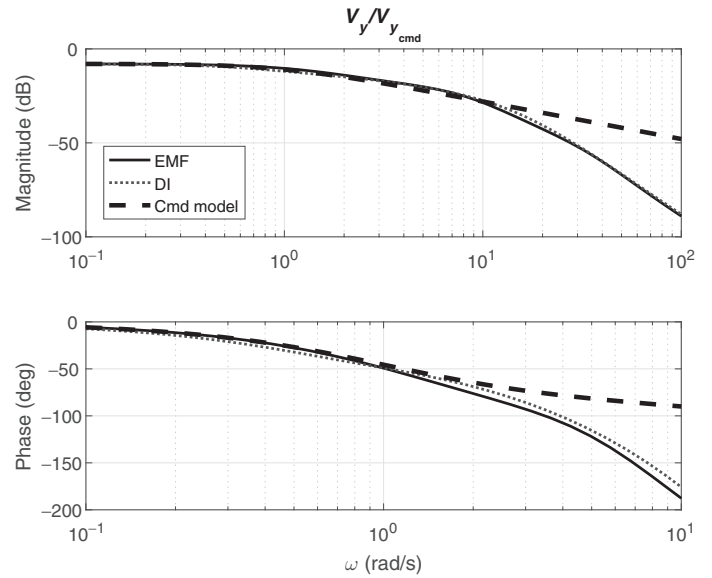
are wholly contained within the Level 1 region. The disturbance rejection performance robustness of the EMF and DI controllers is shown in Fig. 23 for the attitude loop.

Outer loop. Figure 24 shows the outer velocity loop stability margin robustness for both the EMF and DI controllers. For the outer loop, with its lower crossover frequency, there is a larger spread in the confidence ellipsoids as compared to the inner loop. However, the 3σ confidence ellipsoids for both DI and EMF controllers are within the Level 1 region of the specification. In addition, the EMF controller confidence ellipsoids are more compact than the DI controller confidence ellipsoids, suggesting higher robustness to variations in the quadrotor stability and control derivatives. Finally, the disturbance rejection performance robustness of the EMF and DI controllers is shown in Fig. 25 for the velocity loop. There is a similar level of disturbance rejection performance robustness
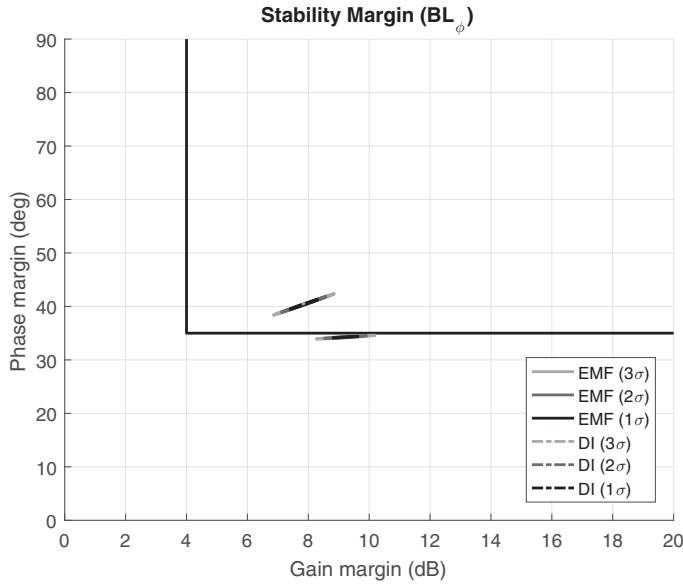
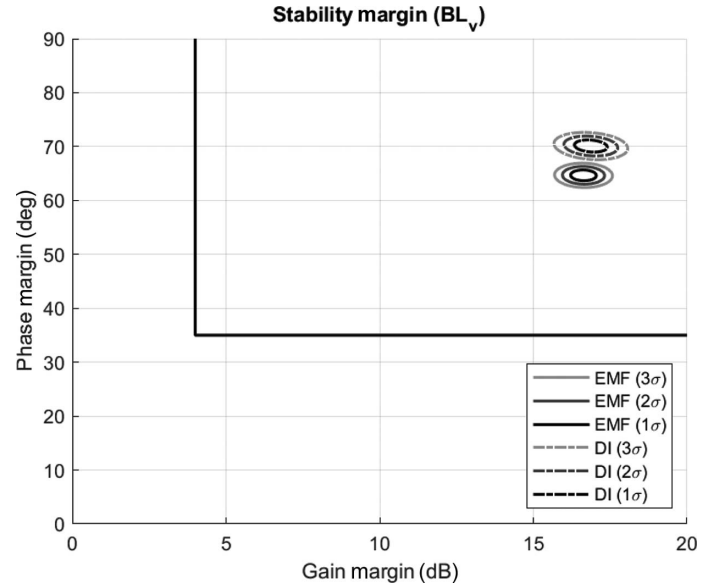**Fig. 22. Inner attitude loop stability robustness.**

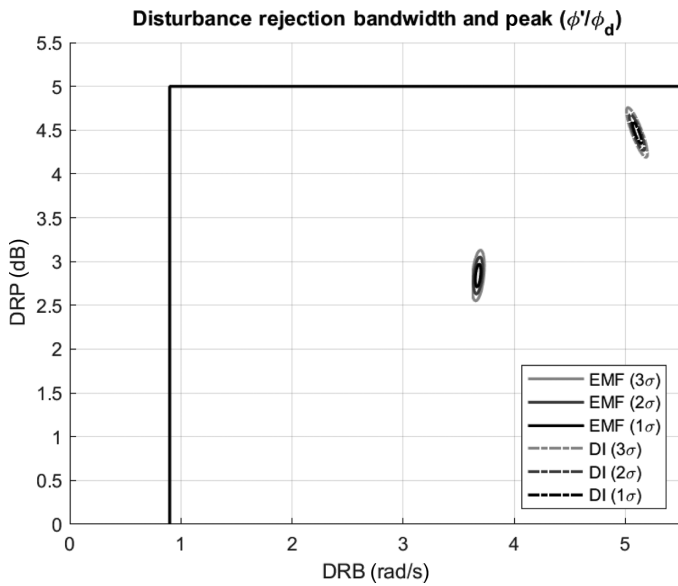**Fig. 24. Outer velocity loop stability robustness.**

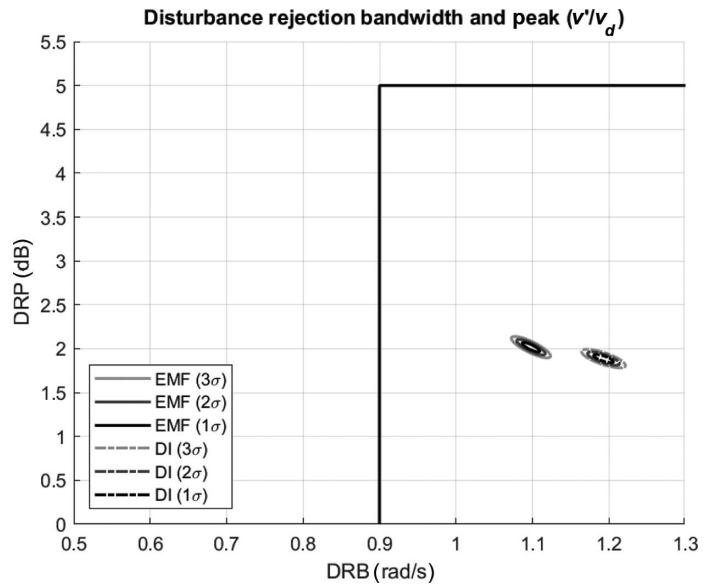**Fig. 23. Inner attitude loop performance robustness.**

Fig. 25. Outer velocity loop performance robustness.

in the inner and outer loops for the both controllers, as seen by the similarly sized confidence ellipsoids.

Conclusions

A parametric model of a quadrotor assembled with commercial off-the-shelf components was identified from flight-test data using a two-step process. First, frequency responses of the aircraft output were extracted from frequency–sweep flight data. Second, state-space models were identified from the frequency response data. The identified model was validated both in frequency and time domains. The bare-airframe dynamics of the identified system were assessed by computing its eigenvalues. Next, DI and EMF controllers were designed for both inner attitude loop and outer velocity loop for the quadrotor. Finally, a novel approach based on an unscented transform was developed and used to

evaluate stability and performance robustness statistics from the identified bare-airframe parameters uncertainty statistics. Based on this work, the following conclusions can be reached:

1) Given the largely decoupled dynamics at low speed, system identification was performed separately on each axis. Overall, the identified model matched the flight data closely in both the frequency and time domain. This indicates that the assumptions of linearity and decoupling of each axis are justified in hover conditions for this type of configuration.

2) The identified model contained a classical hovering cubic in both roll and pitch axes. The similarity between the eigenvalues in roll and pitch is due to the symmetry of the configuration.

3) DI and EMF performances were compared both in the time and frequency domains. Both time and frequency responses show an outstanding match between the two control laws, which were tuned to meet the same requirements. Overall, the gain and phase margins, disturbance

rejection performance, and model following performance for the inner and outer loops of both DI and EMF are satisfactory and match closely to each other.

4) Through the unscented transform, only $2n$ evaluations are done to assess the robustness of the controller through the statistics of the stability margins, DRB, and DRP. Once the $2n$ values of gain and phase margins, DRB, and DRP are computed, they are used to draw 1σ, 2σ, and 3σ confidence ellipsoids on the specifications. The results of the stability and performance robustness analyses showed similar outer-loop stability robustness and inner- and outer-loop performance robustness for both the DI and EMF controllers. Higher inner-loop stability robustness was seen for the EMF controller.

References

[1]Horn, J. F., "Non-Linear Dynamic Inversion Control Design for Rotorcraft," *Aerospace*, Vol. 6, (3), 2019, pp. 38, DOI: 10.3390/aerospace6030038.

[2]Caudle, D. B., Horn, J. F., Keller, E., Thaiss, C., and McColl, C. C., "Damage Mitigating on a Large Rotorcraft Using Load Alleviating Flight Control Laws," AIAA 2015-2549, Proceedings of the AIAA Atmospheric Flight Mechanics Conference, Dallas, TX, June 22–26, 2015, DOI: 10.2514/6.2015-2549.

[3]Sahani, N. A., and Horn, J. F., "Adaptive Model Inversion Control of a Helicopter with Structural Load Limiting," *Journal of Guidance, Control, and Dynamics*, Vol. 29, (2), 2006, pp. 411–420, DOI: 10.2514/1.13391.

[4]Horn, J. F., and Sahani, N. A., "Detection and Avoidance of Main Rotor Hub Moment Limits on Rotorcraft," AIAA 2001-4138, Proceedings of the AIAA Atmospheric Flight Mechanics Conference and Exhibit, Montreal, Canada, August 6–9, 2001, DOI: 10.2514/6.2001-4138.

[5]Geiger, B. R., "Flight Control Optimization on a Fully Compounded Helicopter with Redundant Control Effectors," Master's Thesis, The Pennsylvania State University, University Park, PA, May 2005.

[6]Spires, J. M., and Horn, J. F., "Multi-Input Multi-Output Model-Following Control Design Methods for Rotorcraft," Proceedings of the 71st Annual Forum of the American Helicopter Society, Virginia Beach, VA, May 5–7, 2015.

[7]Saetti, U., and Horn, J. F., "Rotorcraft Simulations with Coupled Flight Dynamics, Free Wake, and Acoustics," Proceedings of the 72nd Annual Forum of the American Helicopter Society, West Palm Beach, FL, May 16–19, 2016.

[8]Saetti, U., "Rotorcraft Simulations with Coupled Flight Dynamics, Free Wake, and Acoustics," Master's Thesis, The Pennsylvania State University, University Park, PA, August 2016.

[9]Pappu, V. S. R., Liu, Y., Horn, J. F., and Cooper, J., "Wind Gust Estimation on a Small VTOL UAV," Proceedings of the 7th American Helicopter Society Technical Meeting on VTOL Unmanned Aircraft Systems and Autonomy, Mesa, AZ, January 24–26, 2017.

[10]Cooper, J., Pappu, V. S. R., Liu, Y., and Horn, J. F., "Vehicle Modeling for Flight Test Measurements of Ship Airwake Disturbances," Proceedings of the 72nd Annual Forum of the American Helicopter Society, West Palm Beach, FL, May 16–19, 2016.

[11]Tischler, M. B., Berger, T., Ivler, C. M., Mansur, M. H., Cheung, K. K., and Soong, J. Y., *Practical Methods for Aircraft and Rotorcraft Flight Control Design: An Optimization-Based Approach*, American Institute of Aeronautics and Astronautics, Inc., Reston, VA, 2017, DOI: 10.2514/4.104435.

[12]Wei, W., Tischler, M. B., and Cohen, K. B., "System Identification and Controller Optimization of a Quadrotor Unmanned Aerial Vehicle in Hover," *Journal of the American Helicopter Society*, **62**, 042007 (2017), DOI: 4050/JAHS 62.042007.

[13]Juhasz, O., Lopez, M. J. S., Berrios, M. G., Berger, T., and Tischler, M. B., "Turbulence Modeling of a Small Quadrotor UAS Using System Identification from Flight Data," Proceedings of the 7th American Helicopter Society Technical Meeting on VTOL Unmanned Aircraft Systems and Autonomy, Mesa, AZ, January 24–26, 2017.

[14]Berrios, M. G., Berger, T., Juhasz, O., and Sanders, F. C., "Hover Flight Control Design for UAS using Performance-Based Disturbance Rejection Requirements," Proceedings of the 73rd Annual Forum of the American Helicopter Society, Fort Worth, TX, May 9–11, 2017.

[15]Cheung, K. K., Wagster, J. A., Tischler, M. B., Ivler, C. M., Berrios, M. G., Berger, T., Juhasz, O., Tobias, E. L., Goerzen, C. L., Barone, P. S., Sanders, F. C., Lopez, M. J. S., and Lehman, R. M., "An Overview of the U.S. Army Aviation Development Directorate Quadrotor Guidance, Navigation, and Control Project," Proceedings of the 73rd Annual Forum of the American Helicopter Society, Fort Worth, TX, May 9–11, 2017.

[16]Mavris, D., DeLaurentis, D., and Soban, D., "Probabilistic Assessment of Handling Qualities Characteristics in Preliminary Aircraft Design," AIAA 98-0492, Proceedings of the 36th Aerospace Sciences Meeting and Exhibit, Reno, NV, January 12–15, 1998, DOI: 10.2514/6.1998-492.

[17]Cooper, J., DeVore, M. D., Reed, A., and Klyde, D., "Handling Quality Analysis and Control Design Using Polynomial Chaos Model-Based Uncertainty Methods," Proceedings of the 75th Annual Forum of the American Helicopter Society, Philadelphia, PA, May 13–15, 2019.

[18]Julier, S. J., Uhlmann, J. K., and Durrant-Whyte, H. F., "A New Approach for Filtering Nonlinear Systems," Proceedings of 1995 American Control Conference, Seattle, WA, June 21–23, 1995, DOI: 10.1109/acc.1995.529783.

[19]Tischler, M. B., and Rample, R. K., *Aircraft and Rotorcraft System Identification*, 2nd ed., American Institute of Aeronautics and Astronautics, Inc., Reston, VA, 2012, DOI: 10.2514/4.868207.

[20]McRuer, D. T., Graham, D., and Ashkenas, I., *Aircraft Dynamics and Automatic Control*, Princeton University Press, Princeton, NJ, 1990, DOI: 10.1515/9781400855988.

[21]Stevens, B. L., Lewis, F. L., and Johnson, E. N., *Aircraft Control and Simulation: Dynamics, Controls Design, and Autonomous Systems*, 3rd ed., John Wiley and Sons, Inc., New York, NY, 2015, DOI: 10.1002/9781119174882.

[22]Bryson, A. E., and Ho, Y., *Applied Optimal Control*, Routledge, New York, NY, 2018, DOI: 10.1201/9781315137667.

[23]Berger, T., Ivler, C. M., Berrios, M. G., Tischler, M. B., and Miller, D. G., "Disturbance Rejection Handling Qualities Criteria for Rotorcraft," Proceedings of the 72nd Annual Forum of the American Helicopter Society, West Palm Beach, FL, May 16–19, 2016.

[24]Stein, G., "Respect the Unstable," *IEEE Control Systems Magazine*, Vol. 23, (4), 2003, pp. 12–25, DOI: 10.1109/MCS.2003.1213600.